J Adv Ceram

Research Article

Facilitating structural strengthening and electromagnetic wave absorption functionalization of dual-phase SiC ceramics via MBNS-dominated multiphase reinforcement strategy

Yang Xia[1,2,3,†], Ming-Xuan Wu[1,2,†], Jun-Tong Huang[1,2,✉], Ruo Huang[4], Dong-Hai Ding[5], Jie Yin[3], Chang-Ming Xu[6], Hui-Yong Yang[1,2], Qi-Fa Wan[2], Lian-Yi Wang[7], Bing-Liang Liang[1,2], Zi-Cui Lu[2], Rui-Ying Luo[1,2]

Cite this article: Xia Y, Wu M-X, Huang J-T, et al. *J Adv Ceram* 2026, **15**(2): 9221234. https://doi.org/10.26599/JAC.2025.9221234

ABSTRACT: Multilayer boron nitride nanosheets (BNNSs) are promising two-dimensional structure–function enhancers due to their structural and mechanical similarity to multilayer graphene (MLG). However, challenges in scalable synthesis/preparation techniques and effective interfacial integration approaches for BNNSs have limited their application in ceramic-matrix composites. Herein, we report the cost-effective, large-scale production of high-quality MBNSs via three-roll milling and their incorporation into a dual-phase SiC matrix through a tailored interfacial modification strategy. These MBNS-dominated microstructures activated multiple synergistic toughening mechanisms, yielding an ~95% increase in flexural strength and an ~50% enhancement in fracture toughness. Additionally, the composite exhibited excellent electromagnetic absorption performance, achieving a minimum reflection loss (RL_{min}) of −52.59 dB at 1.22 mm and a maximum effective absorption bandwidth (EAB_{max}) of full Ku-band coverage (5.6 GHz) at 1.09 mm thickness. This work presents a scalable strategy for the fabrication of high-performance, structurally and functionally integrated composites, offering significant potential for advanced structural and electromagnetic applications.

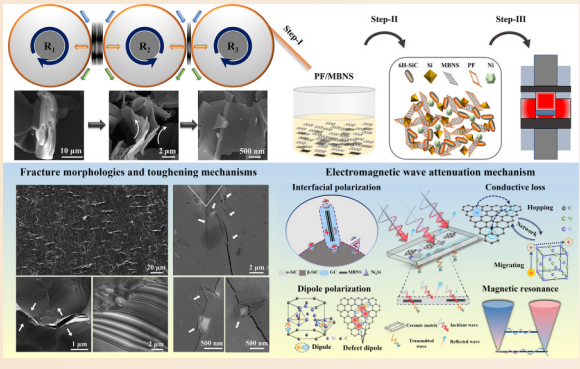

KEYWORDS: multilayer boron nitride nanosheets; three-roll milling; SiC composite ceramic; mechanical properties; electromagnetic wave absorption performance

1 Introduction

Multilayer graphene (MLG) or graphite nanoplatelets (GNPs) have revolutionized two-dimensional (2D) reinforcement strategies in high-performance composites due to their exceptional mechanical, chemical, and electrical properties [1,2]. Despite decades of research into alternative 2D materials, MLG remains the primary choice for 2D reinforcement, largely due to the limited availability of competing phases that offer comparable mechanical robustness and physicochemical stability. Although other emerging 2D materials, such as MXene, MoS_2, and V_2O_5, exhibit excellent electrochemical properties, their low strength and poor structural stability hinder their effectiveness as reinforcement fillers [3,4].

Boron nitride nanosheets or multilayer boron nitride nanosheets (BNNS or MBNS, defined here as 2–10 nm in thickness) have long been regarded as structural analogs to MLG, owing to their similar lattice parameters and layered morphology [5]. Notably, single-layer hexagonal boron nitride (h-BN) has an effective energy release rate nearly an order of magnitude greater than the Griffith criterion and even surpasses that of MLG [6]. This finding highlights the strong potential of MBNS as a toughening agent in composite systems. However, MBNSs have not yet achieved widespread adoption, primarily due to three key

† Yang Xia and Ming-Xuan Wu contributed equally to this study.

[1] Jiangxi Key Laboratory of Lightweight Composite Materials, Nanchang Hangkong University, Nanchang 330063, China. [2] School of Materials Science and Engineering, Nanchang Hangkong University, Nanchang 330063, China. [3] State Key Laboratory of High Performance Ceramics, Shanghai Institute of Ceramics, Chinese Academy of Sciences, Shanghai 200050, China. [4] Pingxiang Huicheng Precision Electromechanical Co., Ltd., Pingxiang 337000, China. [5] College of Materials Science and Engineering, Xi'an University of Architecture and Technology, Xi'an 710055, China. [6] Ji'an Nutpool Materials Technology Co., Ltd., Ji'an 343000, China. [7] School of Materials Science and Engineering, Beihang University, Beijing 100191, China.

✉ Corresponding author. E-mail: huangjt@nchu.edu.cn

Received: September 18, 2025; Revised: November 20, 2025; Accepted: December 22, 2025

challenges: (i) conventional chemical synthesis routes struggle to produce high-crystallinity 2D h-BN structures and typically involve high cost and complex postprocessing [7]; (ii) arising from ionic-like bonding, stronger interlayer interactions in h-BN compared to graphite severely hinder exfoliation by conventional methods (such as ball milling, chemical intercalation, and ultrasonication), resulting in low yield and poor structural retention [8,9]; (iii) the lack of effective surface modification strategies limits interfacial bonding with matrices, reducing load-transfer efficiency.

To date, MBNS reinforcement fillers have been successfully utilized in polymer and metal matrix composites to enhance mechanical strength, thermal conductivity, and dielectric properties [10–12]. In contrast, their application in ceramic matrix composites remains limited, largely due to weak interfacial bonding, stringent dispersion requirements, and the harsh processing environments of ceramic systems [13]. For instance, in SiC-based ceramic composites, the inherent chemical inertness of both the matrix and h-BN often leads to weak interfacial interactions when introducing h-BN fillers without pretreatment, thereby compromising the composites' mechanical performance. Furthermore, ultrahigh sintering temperatures and poor powder flowability severely compromise the structural stability of MBNSs, leading to a nonuniform distribution of reinforcement fillers within the matrix and high-temperature detrimental agglomeration [14].

Overcoming these challenges to enable the incorporation of MBNS reinforcement phases into ceramic systems without compromising matrix strength or functional performance remains a major obstacle. Previously, our group proposed a novel ceramic reinforcement strategy that integrated compositionally diverse reinforcement phases across multiple dimensions (0D, 1D, 2D) and scales (micro/nano) to synergistically strengthen and toughen ceramic matrices [15]. Given its high degree of compositional design freedom, this strategy offers a promising route to overcome the application barriers of MBNS and expand their multifunctional capabilities in ceramic composites.

Guided by this strategy, we developed an advanced scalable and cost-effective mechanical exfoliation process based on three-roll milling (TRM) to produce high-quality MBNS while preserving structural integrity from bulk h-BN raw materials in a resin medium [16]. The exfoliated MBNSs were then uniformly dispersed and assembled with a SiC ceramic matrix via a tailored precursor conversion and powder granulation protocol. To achieve robust interfacial bonding between the MBNSs and the ceramic matrix, the exfoliation medium was retained and selectively dissolved in a polar organic solvent, followed by the *in situ* formation of composite reinforced phase precursors. These were homogenized with ceramic powders, freeze-dried to prevent nanosheet agglomeration, and processed into composite granules through low-temperature organic residue removal. During sintering, the precursors transformed into multiphase reinforcements (β-SiC, 0D Ni_2Si particles, 0D glassy carbon (GC)) uniformly distributed within the α-SiC matrix. These phases demonstrated dual functionality: i) forming dual-phase α/β-SiC (DS) through a self-association reaction and ii) establishing chemical bonds with MBNSs, promoting horizontal alignment and integrated assembly of the composite. The resulting MBNS-reinforced DS composite (DS@MBNS) exhibited multiple architectures that facilitated effective load transfer and significant mechanical reinforcement. Comparative analysis confirmed the superior toughening efficiency of exfoliated MBNS over pristine counterparts, achieving performance on par with GNP.

Realizing the functionalization of structural ceramics with high mechanical performance is critical for demanding engineering applications in extreme environments such as aero-engine blades, nozzle cavity liners, precision bearings, and radiation-resistant architectures [17,18]. These systems require not only excellent mechanical reliability to ensure service reliability but also multifunctional performance metrics to address interdisciplinary requirements. To assess the application potential of DS@MBNS composites, we systematically investigated both their mechanical behavior and electromagnetic properties. Remarkably, the composites exhibited favorable electromagnetic absorption performance, a property rarely achieved in dense, nonmetamaterial ceramic systems, demonstrating the promise of structurally functionalized ceramics for advanced applications.

2 Experimental

2.1 Raw materials

Alpha silicon carbide (α-SiC, 1–2 μm, purity ≥ 99.9%, Shanghai Macklin Technology Co.), commercially available phenolic-formaldehyde (PF) resin (thermosetting PF 900A1; Hebei Zetian Chemical Co., Ltd., China), hexagonal boron nitride (h-BN) (CG25, 20–30 μm, Ji'an Nutpool Materials Technology Co., Ltd. China), silicon powder (~1 μm, purity ≥ 99.96%, Chuangying Metal Materials Co., Ltd., China), boron carbide (B_4C) (~1 μm, purity ≥ 99.9%, Bisley New Materials Co., Ltd., China) and $Ni(NO_3)_2{\cdot}6H_2O$ (AR, Xilong Science Co., Ltd., China) were used as raw materials. 5-(hydroxymethyl) furan-2-carbaldehyde (5F2C, Shanghai BiDe PharmaTech Co., Ltd., China) was used as an organic polar solvent to dissolve PF.

2.2 Fabrication of 2D nanosheets and DS@MBNS composites

The fabrication of MBNS-reinforced dual-phase α/β-SiC composites (DS@MBNS) involved three key stages. Detailed formulations are provided in Table S1 in the Electronic Supplementary Material (ESM). The procedure was as follows:

(i) Exfoliation of 2D MBNS (Fig. S1(a) in the ESM): A precise amount of phenolic resin (PF) was premixed with h-BN feedstock. The mixture was subsequently processed via structure-preserving mechanical exfoliation using three-roll milling (TRM), applying 24 programmed differential roller shearing cycles (Table S2 in the ESM) to achieve high-yield MBNS production. The resulting slurry, containing uniformly dispersed MBNS within the PF matrix (Fig. S2 in the ESM), was collected for subsequent processing.

(ii) Preparation of DS@MBNS composite ceramic powder (Fig. S1(b) in the ESM): The PF/MBNS slurry was first solvated in 5F2C solvent under magnetic stirring for 1 h, followed by sequential addition of nickel nitrate catalyst, boron carbide sintering aid and silicon powder with high-shear homogenization for 6 h to form the composite reinforcement precursor. Subsequently, α-SiC powder was introduced for continued homogenization for 6 h. The slurry was cryo-stabilized below −5 °C for 12 h and then lyophilized to eliminate water. Residual solvent was removed at 180 °C, yielding composite ceramic granules (Fig. S1(c) in the ESM).

(iii) Sintering densification: Composite powders were loaded into a graphite die assembly (Φ50 mm, carbon felt insulated) and densified under vacuum following a multistage temperature–pressure schedule: room temperature to 700 °C at 50 °C/min under 15 MPa; 700–1000 °C at 50 °C/min under

15 MPa (0.5 h hold); 1000–1450 °C at 50 °C/min under 15 MPa (2 h hold); 1450–1950 °C at 50 °C/min under 50 MPa (0.5 h hold); followed by controlled depressurization (2 min ramp to 0 MPa) and furnace cooling.

The specimens were designated OS, DS, DS@2BN, DS@1MBNS, DS@2MBNS, and DS@4MBNS, corresponding to single-phase α-SiC, dual-phase SiC, dual-phase SiC loading of 2% h-BN or 1%, 2%, and 4% MBNS by mass relative to the total composite weight. The OS, DS, and DS@2BN groups served as controls. The OS specimen preparation process was as follows: step (i) was omitted. In step (ii), B_4C powder was added to deionized water and stirred magnetically for 1 h, followed by the gradual addition of α-SiC powder and high-speed dispersion for 6 h. The mixture then underwent freeze granulation using the same procedure. The DS specimen was also prepared by omitting step (i). In step (ii), the PF/MBNS slurry was replaced with PF only, while all other operations remained unchanged. For the DS@2BN specimen, step (i) was also omitted. In step (ii), the PF/MBNS slurry was substituted with PF/BN, with subsequent step (iii) unchanged.

2.3 Material characterizations

The phase compositions of the composite ceramics were examined using an X-ray diffractometer (XRD; D8 ADVANCE-A25, Germany; Cu Kα, λ = 0.15406 nm). Morphologies and microstructures were observed and characterized using a field emission scanning electron microscope (FESEM; Nova Nano SEM450, FEI, USA) and a transmission electron microscope (TEM; JEM-210, JEOL, Japan), complemented by selected-area electron diffraction (SAED) and energy-dispersive spectroscopy (EDS).

To characterize the exfoliated MBNS, PF residues were removed by ultrasonic cleaning and high-speed centrifugation in ethanol (AR grade). The topography and height profile of exfoliated MBNS were captured using an atomic force microscope (AFM; SPA400, NSK Ltd., Japan). A fast hot-press sintering furnace (FHPS-858, Suzhou Haatn Technology Co., Ltd., China) was utilized for the sintering and preparation of composite ceramics. The molecular structures and bonding states of the specimens were analyzed using a Raman scattering spectroscope (JY LabRAM HR Evolution, HORIBA, Japan, 532 nm laser) over a wavenumber range of 50–4000 cm^{-1}. The surface elemental composition, chemical valence, and bonding states were characterized via an X-ray photoelectron spectroscope (XPS; ESCALAB250, Thermo VG, USA). The hardness of polished ceramic specimens was measured using a Vickers hardness tester (ZHVS-1000ATE), with at least seven indentations per sample to calculate the average Vickers hardness (H_V). The loading direction was aligned perpendicular to the hot-press axis.

2.4 Three-point bending and single edge V-notch beam tests

The mechanical properties of the specimens were evaluated using a microcomputer-controlled electronic universal testing machine (WDW-50C, Hualong Testing Instruments Co., Ltd., China). Beam-shaped specimens were machined from hot-pressed billet samples with a 50 mm diameter for three-point bending (40 mm length × 4 mm width × 3 mm thickness) and single-edged V-notched beam (SEVNB; 40 mm length × 3 mm width × 4 mm thickness) testing, with the specimen width direction perpendicular to the hot-press loading axis. For SEVNB specimens, a notch of 0.6±0.2 mm depth was introduced along the thickness direction using a 250 μm diamond abrasive tip, followed by diamond paste polishing and razor blade sharpening to ensure a sharp notch. All specimens were polished and edge-chamfered with sandpaper to minimize machining-induced surface defects. During tests, the indenter speeds were set to 0.5 mm·min^{-1} for three-point bending and 0.01 mm·min^{-1} for SEVNB tests, with a fixed support span of 30 mm. Mechanical properties were calculated from displacement–load curves via posttest analysis.

The fracture toughness (K_{IC}) can be calculated using Eqs. (1) and (2) [19]:

$$K_{IC} = \frac{P_m S}{Bw\frac{3}{2}} f\left(\frac{a}{w}\right) \tag{1}$$

$$f\left(\frac{a}{w}\right) = \frac{3}{2}\left(\frac{a}{w}\right)^{\frac{1}{2}} \times \frac{\left\{1.99 - \left(\frac{a}{w}\right)\left(1-\frac{a}{w}\right)\left[2.15 - 3.93\frac{a}{w} + 2.7\left(\frac{a}{w}\right)^2\right]\right\}}{\left(1+\frac{2a}{w}\right)\left(1-\frac{a}{w}\right)^{\frac{3}{2}}} \tag{2}$$

where P_m is the maximum load value from the displacement–load curve in the SEVNB test, S is the support span, B is the thickness of the sample, w is the width, a is the notch depth, and $f(\frac{a}{w})$ represents the stress intensity shape factor.

The error bars were plotted using the sample standard deviation formula (Eq. (3)):

$$s = \sqrt{\frac{1}{n-1}\sum_{i=1}^{n}(\bar{x} - x_i)^2} \tag{3}$$

where n denotes the number of data points, x_i represents the ith data point, $\bar{x}$ is the sample mean, and s is the sample standard deviation. Data are presented as the mean±standard deviation from three independent replicates (n = 3).

2.5 Dielectric and magnetic properties test

The composite ceramics were machined into specimens measuring 15.8 mm × 7.9 mm × 3.0 mm. The relative complex permittivity ($\varepsilon_r = \varepsilon' - j\varepsilon''$) and relative complex permeability ($\mu_r = \mu' - j\mu''$) of the specimens were measured using the waveguide method within the Ku-band frequency range of 12.4–18.00 GHz on a vector network analyzer (VNA; 3672B-S, Electric Instrument Co., Ltd., China). Room-temperature magnetic hysteresis loops were acquired using a liquid-helium-free integrated physical property measurement system (PPMS; DynaCool, Quantum Design, USA) to evaluate saturation magnetization (M_s) and coercivity (H_c).

The reflection loss (RL) was calculated using Eqs. (4) and (5) [20]:

$$RL = 20\lg\left|\frac{Z_{in} - 1}{Z_{in} + 1}\right| \tag{4}$$

$$Z_{in} = \sqrt{\frac{\mu_r}{\varepsilon_r}}\tanh\left(j\frac{2\pi f d}{c}\sqrt{\mu_r\varepsilon_r}\right) \tag{5}$$

where Z_{in}, ε_r, and μ_r represent the normalized input impedance, relative permittivity, and relative permeability, respectively, and f, d, and c denote the electromagnetic wave frequency, absorber thickness, and speed of light in vacuum, respectively.

3 Results and discussion

3.1 Procedure design of multilayer boron nitride nanosheets and DS@MBNS composites

The scalable production of structurally intact multilayer boron nitride nanosheets (MBNS) through cost-effective and environmentally friendly methods remains a significant challenge. While traditional approaches such as conventional mechanical exfoliation, liquid-phase separation, and chemical synthesis methods offer partial benefits, they universally fail to achieve an optimal balance among production scale, cost efficiency, and structural integrity. Furthermore, the intrinsically high surface energy and strong interlayer van der Waals interactions of 2D nanosheets present persistent difficulties for achieving uniform dispersion within ceramic matrices. To address these limitations, we developed an improved exfoliation strategy that builds upon our previous methodology [15,16,21]. Specifically, we employed a high-viscosity phenolic resin (PF) as a protective medium in combination with a three-roll milling (TRM) process. Rather than pursuing a bottom–up synthesis route, our approach used low-cost, unmodified bulk h-BN feedstock (20–30 μm) and was subjected to gradual layer-by-layer delamination via precision mechanical shearing (Fig. 1(a)). This protective exfoliation method enabled high-yield production of nanoscale MBNS (Figs. S3(a)–S3(d) in the ESM) with controlled thickness (~5 nm, confirmed by AFM; Figs. S3(e) and S3(f) in the ESM) while ensuring uniform dispersion in the PF medium. XRD and FT-IR analyses verified that the phase composition and molecular integrity were retained postexfoliation (Figs. S3(g) and S3(h) in the ESM). A distinct leftward shift in the (002) diffraction peak suggested interlayer expansion along the *c*-axis, which was quantitatively confirmed by TEM measurements showing increased *d*-spacing (d_{MBNS} = 0.346 nm vs. $d_{h\text{-}BN}$ = 0.333 nm, Figs. S3(i) and S3(j) in the ESM) [22].

To promote strong interfacial bonding between the MBNSs and the SiC ceramic matrix, we designed a composite reinforcement phase precursor system by introducing silicon powder and nickel nitrate into the PF/MBNS mixture via organic polar solvent-assisted processing. This mixture was then combined with commercial α-SiC powders, followed by freeze granulation and low-temperature solvent removal to yield

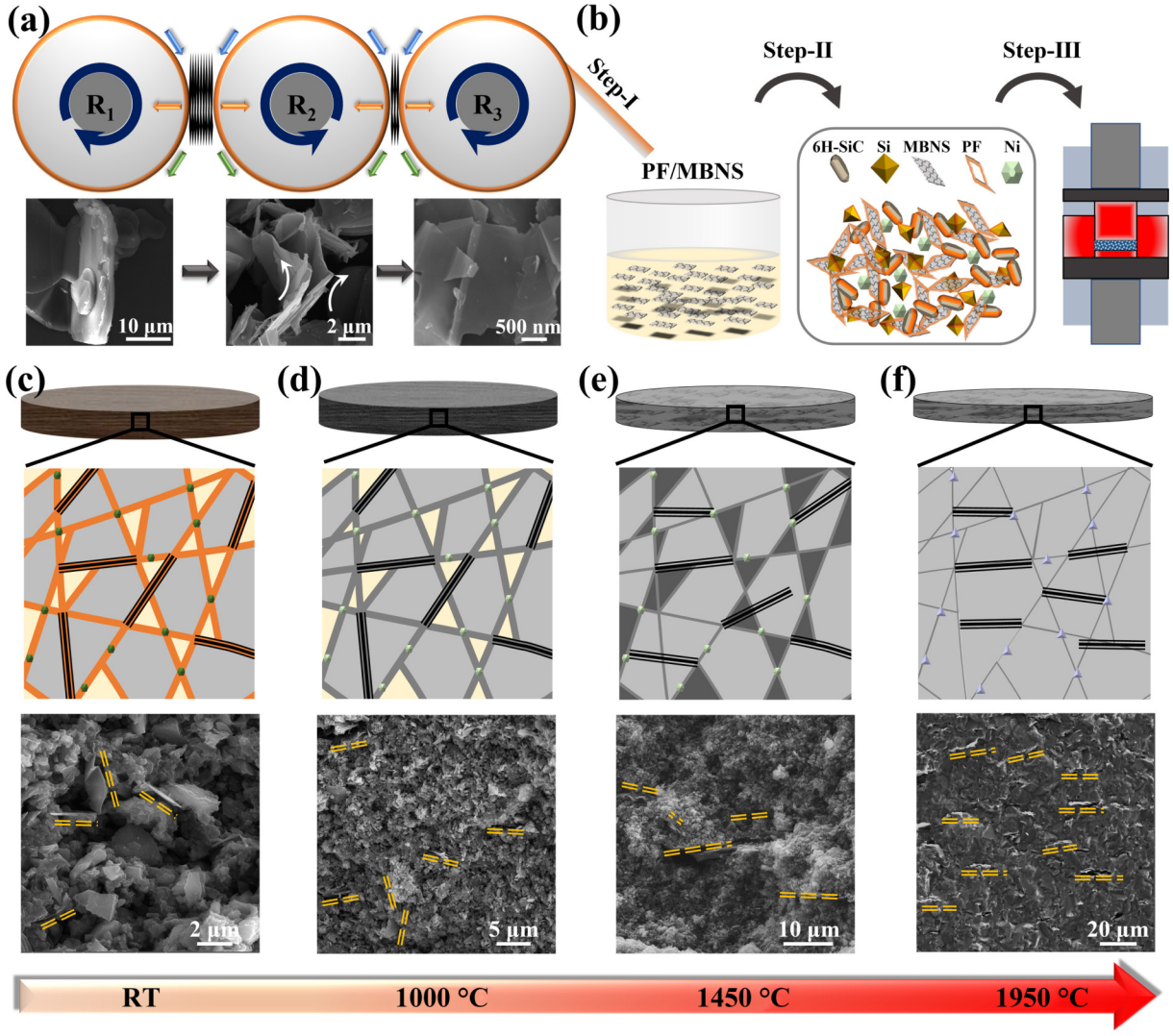

Fig. 1 Fabrication process and microstructure evolution of DS@MBNS composites. (a) Schematic overview of the TRM exfoliation process for h-BN feedstock. SEM images from left to right show the untreated h-BN, the BN flakes after 12 exfoliation cycles, and the MBNS after 24 exfoliation cycles. (b) Brief flow of powder preparation and rapid hot-press sintering of DS@MBNS composites. (c–f) Diagram of the respective structural evolution and internal morphology of the materials at key temperature stages during the sintering of DS@MBNS composites.

sinterready composite powders for fast hot-press consolidation (Fig. 1(b)). SiC was chosen as the matrix material due to its inherent sintering challenges compared to other ceramics, thereby providing a stringent testbed for evaluating the structural stability and reinforcement efficacy of MBNS under extreme conditions. In contrast to conventional densification-focused sintering protocols, our approach incorporated a transformative precursor activation stage prior to matrix densification, extending our prior inspiration [23]. Initially, rapid heating (50 °C/min) to 1000 °C induced controlled pyrolysis of PF, generating reducing gaseous species that converted nickel nitrate into nanoscale Ni catalysts and carbonaceous residues (Figs. 1(c) and 1(d)). Subsequent thermal treatment at 1450 °C activated Ni-catalyzed reactions between silicon and residual carbon, yielding β-SiC-dominated multiphase structures comprising silicon carbide particles, whiskers, and a minor amount of GC (Fig. 1(e)). Meanwhile, metallic Ni alloyed with Si to form Ni_2Si, an intermetallic compound with a low melting point (< 1400 °C), could create a transient liquid phase during sintering at elevated temperatures [24]. This liquid phase served two functions for enhancing densification kinetics and promoting horizontal alignment of MBNS under uniaxial pressure. Finally, at 1950 °C, the α-SiC matrix was self-combined with β-SiC to form a dual-phase α/β-SiC (DS) matrix and assembled with 2D MBNSs at 1950 °C. Since 0D Ni_2Si/GC formed a well-dispersed state in the DS matrix, for simplicity, we integrated them into the DS matrix description; thus, they resulted in the formation of the MBNS-reinforced DS (DS@MBNS) composites (Fig. 1(f)).

To validate the design rationale and explain the observed performance evolution, we systematically investigated the reinforcement efficacy of h-BN in both pristine and exfoliated forms as well as the influence of the MBNS content. Herein, our approach provides a scalable, structurally protective, and matrix-compatible processing route for MBNS preparation and application. Furthermore, the strategy for incorporating MBNSs into the SiC matrix would demonstrate strong generalizability and hold significant promise for the future development of structurally functional ceramic composites.

The phase compositions of all the sintered specimens were examined via XRD, with the results presented in Fig. 2(a). The control specimen OS maintained single-phase α-SiC, while all modified formulations exhibited dual-phase α/β-SiC signatures (JCPDS #74-1302 for 6H(α)-SiC; #75-0254 for 3C(β)-SiC) [25,26]. This was evidenced by a typical feature with the increased peak intensity in the enlarged XRD region of 34.5°–35.5°, suggesting the presence of stacking faults (SFs) in β-SiC along the (111) plane (as evidenced by the HRTEM in Fig. S4(c) in the ESM), distinguishing the modified specimens from the control specimen OS. A distinct diffraction peak in the 26°–27° range corresponded to the (002) plane of the coexistence of graphitic carbon and h-BN. The graphitic component was attributed to partial graphitization of amorphous carbon residues derived from PF

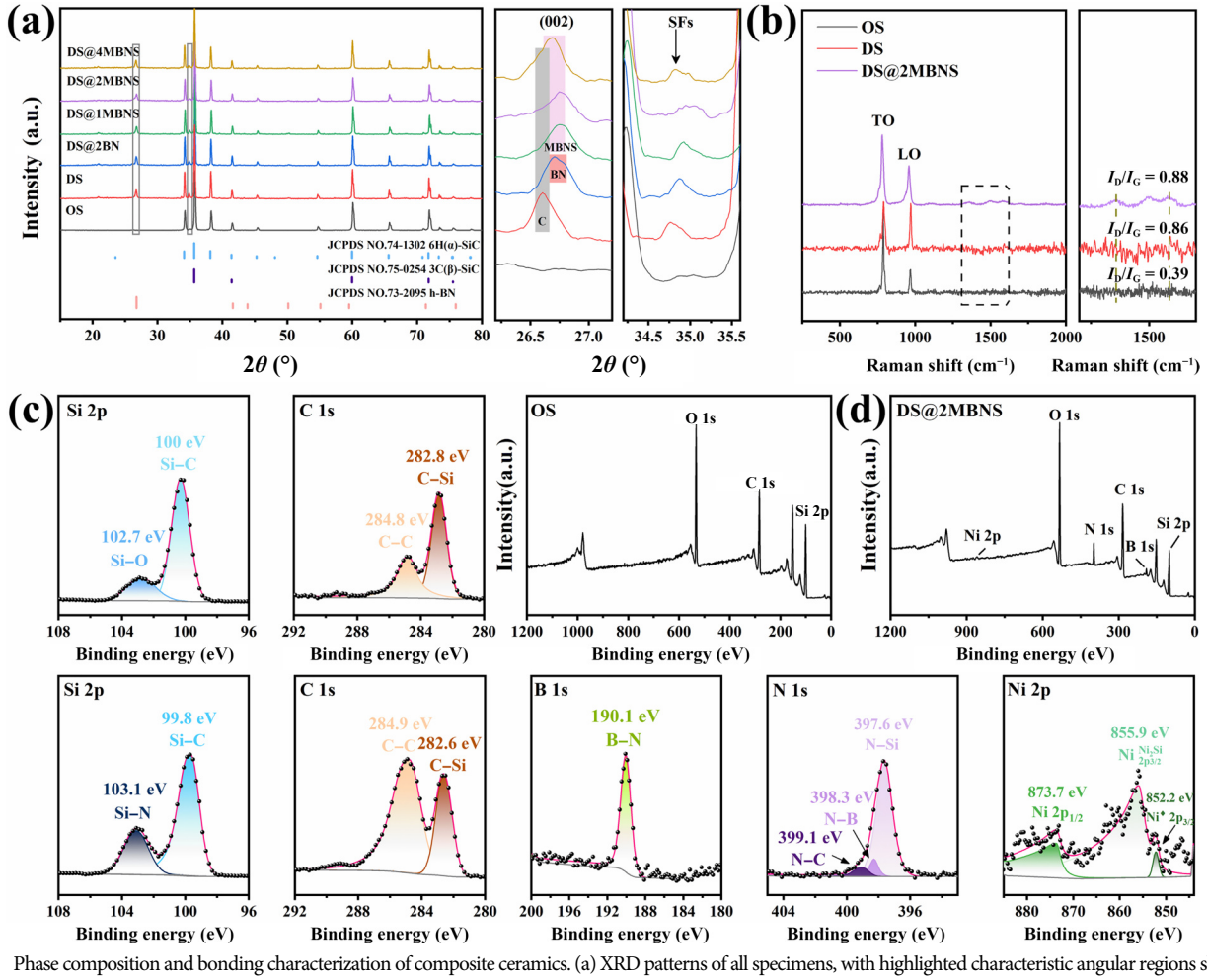

Fig. 2 Phase composition and bonding characterization of composite ceramics. (a) XRD patterns of all specimens, with highlighted characteristic angular regions shown in the right panel. (b) Comparative Raman spectra of OS and DS@2MBNS specimens. (c) XPS survey spectra of OS, alongside high-resolution spectra of Si 2p and C 1s. (d) XPS survey spectra of DS@2MBNS, with high-resolution spectra of Si 2p, C 1s, B 1s, N 1s, and Ni 2p.

catalyzed under high-temperature conditions to yield semicrystalline glassy carbon (GC) [15]. Notably, graphitic ordering appeared more pronounced on the GC side adjacent to Ni_2Si (Fig. S4(b) in the ESM). The persistent h-BN/MBNS peak at ~26.7° confirmed the thermal stability of the BN phase throughout the sintering process. Raman spectral comparisons among OS, DS, and DS@2MBNS specimens revealed that they exhibited the characteristic transverse optical (TO) and longitudinal optical (LO) Si–C vibrational modes at 790 and 970 cm^{-1}, respectively (Fig. 2(b)) [27]. The intensity ratio of the D and G bands (I_D/I_G) increased in the DS (0.86) and DS@2MBNS (0.88) samples compared to OS (0.39), suggesting an increase in structural defects within the carbon phase, likely due to the incorporation of MBNS and GC. The chemical bonding states of the composites were investigated through XPS (Figs. 2(c) and 2(d)). The OS specimen exhibited only Si 2p, C 1s, and O 1s peaks (Fig. 2(c)), consistent with its monophasic composition. The detected oxygen was likely attributed to surface oxidation and adsorbed species. High-resolution spectra revealed that the Si 2p peak could be deconvoluted into Si–C (100 eV) and Si–O (102.7 eV) components, while the C 1s spectra represented the combination of C–Si and C–C bonds. In contrast, the DS@2MBNS specimen displayed a richer spectral profile, with additional peaks for B 1s, N 1s, and Ni 2p (Fig. 2(d)), confirming the successful incorporation of MBNS and Ni-based phases. The high-resolution Si 2p spectrum revealed a new component at 103.1 eV, corresponding to the Si–N bond [28], suggesting a possible chemical interaction between the SiC matrix and MBNS. N 1s deconvolution further identified N–Si (397.6 eV), N–B (398.3 eV), and N–C (399.1 eV) species, with the N–Si peak corroborating the formation of interfacial Si–N bonding. The C 1s spectra of DS@2MBNS also exhibited a stronger C–C signal and broader full width at half-maximum (FWHM), suggesting a higher carbon content and increased defect density, which was consistent with the Raman spectra of the D and G bands (Fig. 2(b)). The B 1s spectrum displayed a single peak corresponding to B–N bonding. Last, the Ni 2p spectra revealed a major characteristic peak at 855.9 eV (Ni^{Ni2Si} $2p^{3/2}$), along with peaks at 852.2 eV (Ni^{*} $2p^{3/2}$) and 873.7 eV (Ni $2p^{1/2}$), confirming the presence of both Ni_2Si and oxidized nickel species [29,30].

The microscale distribution (grain boundary or intracrystalline) and assembly configuration of multiple reinforcement phases within the ceramic matrix are crucial for understanding the composite architecture and explaining property evolution. In the DS@MBNS system, a reinforcement network dominated by MBNS, synergistically aided by Ni_2Si and GC, was identified. Their spatial distribution within the SiC matrix is schematically illustrated in Fig. 3(a). Both Ni_2Si and MBNS predominantly resided at grain boundaries rather than intracrystalline regions (Figs. 3(b) and 3(c)), consistent with their limited involvement in

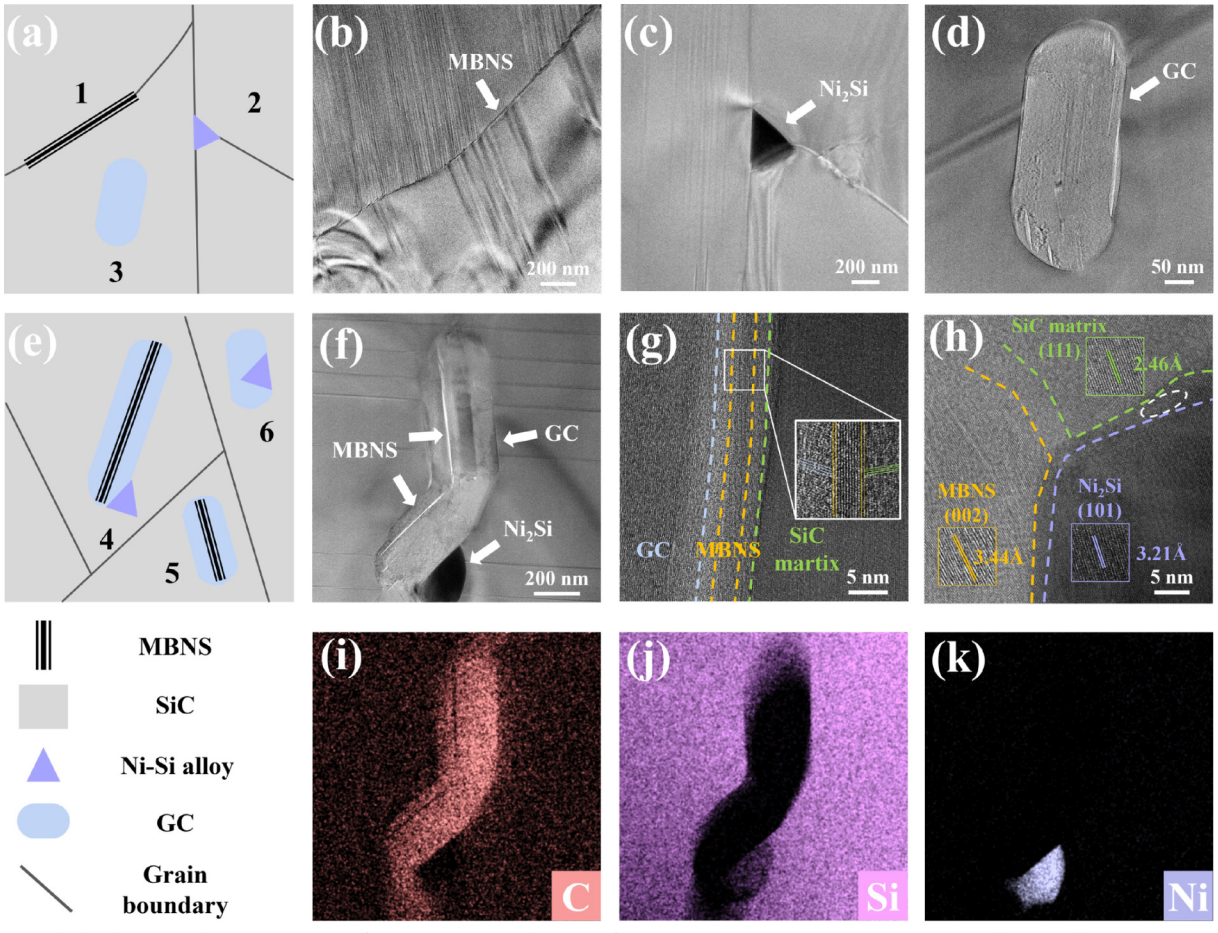

Fig. 3 Spatial distribution and microstructures of MBNS, Ni_2Si, and GC reinforcements in SiC composite ceramics. (a) Schematic illustrating unassembled reinforcement distribution at ceramic grain boundaries versus intracrystalline regions. Representative TEM images of (b) case 1 MBNS, (c) case 2 Ni_2Si, and (d) case 3 GC. (e) Schematic of assembled reinforcement architectures. (f) TEM image of case 4 showing the triphasic assembly of MBNS, GC, and Ni_2Si (cases 5 & 6 shown in Figs. S4(d) and S4(e) in the ESM). (g) HRTEM images highlighting interfacial bonding among GC (light blue), MBNS (yellow), SiC (green) and Ni_2Si (light purple). (h) HRTEM images of the interface between the MBNS, Ni_2Si, and SiC matrix, with coherent lattice regions indicated by white ellipses. (i–k) Elemental mappings of C, Si, and Ni corresponding to (f).

the direct formation of the DS matrix. In contrast, GC, derived from the residual carbon of PF pyrolysis, was directly involved in DS matrix formation and was thus typically encapsulated within a crystalline matrix, forming regular geometries (e.g., rounded rods) under stable environmental conditions (Fig. 3(d)). Assembled reinforcement phases exhibited distinct configuration types, categorized schematically in Fig. 3(e). Case 4 demonstrated GC encapsulating MBNS to form an armor-like protective layer, synergistically combining with adjacent Ni_2Si to create composite reinforcement phases with potential cooperative strengthening effects (Fig. 3(f)). Elemental mapping analyses further provided their structural details (Figs. 3(i)–3(k)). Additional assembly forms were illustrated by Cases 5 and 6, as evidenced in Figs. S4(d)–S4(f) in the ESM, highlighting the diversity and complexity of reinforcement phase integration. Interfacial bonding between reinforcements and the SiC matrix was examined through HRTEM. Figure 3(g) depicts a typical triphasic interface where MBNS was situated between GC and the SiC matrix. The interfacial region exhibited well-defined phase boundaries, with a magnified view of the boxed area revealing tightly bonded interfaces among the three phases. Crystallographic analysis identified the (101) lattice plane of Ni_2Si (3.21 Å), the (002) plane of MBNS (3.44 Å), and the (111) plane of SiC (2.46 Å) (Fig. 3(h)) [31]. Notably, the Ni_2Si/SiC interface exhibited a higher degree of lattice coherence (highlighted by the white ellipse), suggesting superior atomic ordering compared to the other interfaces (yellow–violet and yellow–green zones). This enhanced ordering was likely associated with β-SiC catalytic transformation, suggesting reduced interfacial energy that might facilitate Si atom diffusion and local crystalline growth [32].

3.2 Mechanical properties and toughening mechanisms of DS@MBNS composites

The mechanical properties of the composite ceramics were evaluated via three-point bending and single-edge V-notched beam (SEVNB) methods, with the loading direction applied perpendicular to the in-plane alignment of the MBNS. Full mechanical property data are provided in Table S3. Although all specimens retained the linear stress–strain behavior characteristic of brittle ceramics, the DS@MBNS composites exhibited enhanced ductility compared to conventional ceramics and glasses (Fig. 4(a)) [19,33].

Control groups (OS, DS, DS@2BN) and DS@*x*MBNS variants (x = 1, 2, 4) were systematically compared. The DS matrix specimens demonstrated superior strength and strain ranges versus OS (245±31 MPa, 0.196%±0.004%), while DS@4MBNS achieved the highest enhancements, with a 94.5% increase in flexural strength (477±65 MPa) and a 67.9% increase in strain capacity (0.329%±0.011%). Although the flexural modulus increased modestly across the DS series (Fig. 4(b)), the simultaneous improvement in both strength and strain underscored the composite's ability to accommodate bending deformation, favoring ductile failure over brittle fracture under external loading. Notably, the DS specimen group exhibited concurrent improvements in strength, toughness, and hardness relative to OS (Figs. 4(b)–4(d)), validating the efficacy of the dual-phase SiC matrix strategy. Using DS and DS@2BN as baselines, we compared the performance of DS@*x*MBNS specimens with different MBNS contents. In particular, unexfoliated h-BN reduced the strength/toughness versus DS, confirming the reinforcement limitations of bulk h-BN in the DS matrix. Conversely, DS@2MBNS exhibited superior mechanical performance to both DS@2BN and DS (except fracture toughness in DS). At higher MBNS content, DS@4MBNS exhibited the most comprehensive mechanical enhancement, including a 50.4% increase (reached at 6.02 MPa·m$^{1/2}$) in fracture toughness (K_{IC}) over OS, thereby validating the efficacy of exfoliated MBNS for ceramic reinforcement. It is well established that the mechanical properties of structural ceramics are highly sensitive to the degree of matrix densification [34]. Within the DS@*x*MBNS series, the DS@2MBNS specimen exhibited slightly 1%–2% lower relative densities compared to DS@1MBNS and DS@4MBNS, which was reflected in the anomalous decrease in hardness versus K_{IC} curves (Figs. 4(c) and 4(d)). Traditional structural ceramics often suffer from a stiffness–toughness trade-off, where the incorporation of a secondary phase typically improves either flexural strength or fracture toughness—rarely both—due to the limitations of a single reinforcement mechanism [35]. Benchmarking our MBNS/SiC system against literature-reported graphene nanoplatelet (GNP) or MBNS-reinforced SiC composites (Fig. 4(e)), this work achieved superior mechanical enhancements in both regimes at significantly lower material and processing costs. More importantly, our multiphase reinforcement strategy avoided the typical matrix property degradation (e.g., hardness reduction) observed in single-reinforcement systems, instead delivering an improvement in comprehensive properties (Fig. 4(f)). This level of performance integration remains a major challenge in the field of ceramic reinforcement.

The K_{IC} serves as a critical metric for evaluating a composite's resistance to crack initiation and propagation, which directly determines the engineering reliability of structural ceramics. By observing the cross-sections of the specimens along with the damage traces after external loading, we investigated the self-toughening of the matrix and the synergistic toughening mechanism of the second phase demonstrated by the DS@MBNS composites. At first, the embedded boron nitride nanosheets were frequently observed with near-horizontal alignment in the ceramic matrix, effectively intercepting and deflecting propagating cracks (Fig. 5(a)). In contrast, unexfoliated h-BN, when incorporated at equivalent mass fractions, exhibited a significantly lower spatial distribution due to its larger particle size and reduced processability—by orders of magnitude (Figs. S5(c)–S5(f) in the ESM). These bulk h-BN flakes tend to cause local interfacial mismatch with the matrix, leading to weakened matrix bonding and reduced mechanical performance of the composites [34]. In comparison, exfoliated MBNS, owing to their nanoscale thickness and high aspect ratio, formed intimate interfaces with the SiC matrix and bridged opposing crack faces, generating closure forces that dissipate crack energy upon loading or arrest crack growth upon penetration (Figs. 5(b), Figs. S6(a) and S6(b) in the ESM). Furthermore, the DS matrix itself exhibited a self-toughening effect relative to OS. The fracture surface morphologies in DS revealed step-shaped tearing patterns, in stark contrast to the smooth and planar fracture surfaces of the OS specimen (Fig. 5(c), Figs. S5(a) and S5(b) in the ESM). These tortuous crack paths reflect increased energy consumption and crack propagation resistance, contributing to enhancing the composites' fracture toughness [36]. Moreover, the 0D Ni_2Si and GC particles dispersed within the DS matrix played a crucial role in toughening by promoting microcrack derivation and deflection (Figs. S6(c) and S6(d) in the ESM), which was a primary reason for the superior K_{IC} value in DS.

To further investigate the toughening mechanisms, polished surfaces of the ceramics were subjected to conical diamond indentation. In OS specimens, cracks propagated in straight, singular paths typical of brittle failure. In contrast, the DS@MBNS

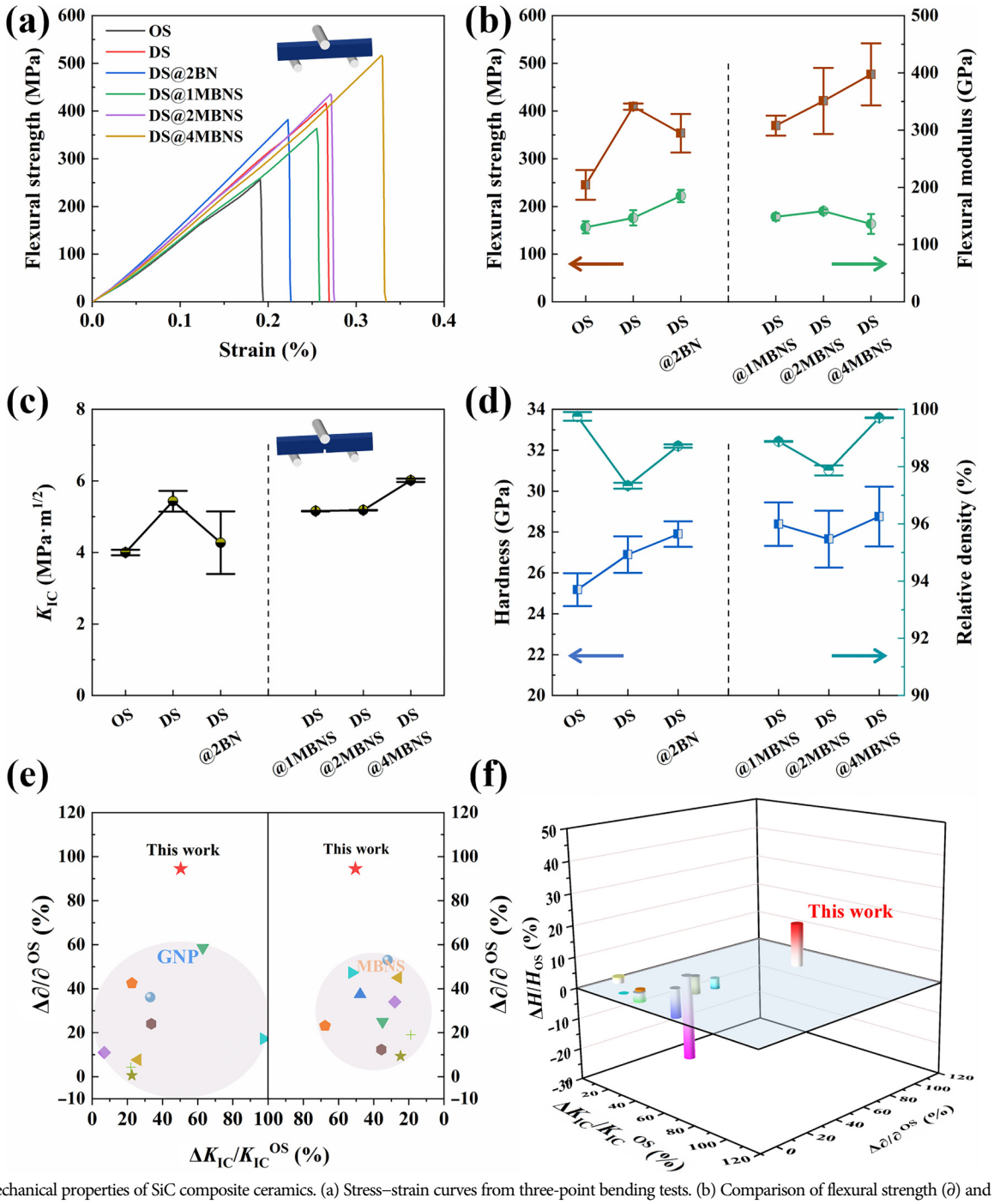

Fig. 4 Mechanical properties of SiC composite ceramics. (a) Stress–strain curves from three-point bending tests. (b) Comparison of flexural strength (∂) and modulus among specimens. (c) Fracture toughness (K_{IC}) analysis. (d) Correlation between Vickers hardness (H) and relative density. (e) Dual-axis comparison of the DS@4MBNS specimen with GNP/MBNS-reinforced ceramic composites, left (GNP system), right (MBNS system). (f) Three-dimensional performance mapping of DS@4MBNS against previously reported GNP/MBNS reinforcement strategies. For references, see Table S4 and S5 in the ESM. Note: $\triangle\partial/\partial^{OS} = (\partial^{DS@4MBNS} - \partial^{OS})/\partial^{OS} \times 100\%$, $\triangle K_{IC}/K_{IC}{}^{OS} = (K_{IC}{}^{DS@4MBNS} - K_{IC}{}^{OS})/K_{IC}{}^{OS} \times 100\%$, $\triangle H/H^{OS} = (H^{DS@4MBNS} - H^{OS})/H^{OS} \times 100\%$. For example, ∂^{OS} and $\partial^{DS@4MBNS}$ represents the flexural strengths of the OS and DS@4MBNS spcimens, respectively, and $\triangle\partial$ denotes the difference in flexural strength between the DS@4MBNS and OS specimens. The other two types of physical quantities related to K_{IC} and H can also be understood by analogy.

composites displayed complex, multibranching crack networks originating from the indentation zone (Fig. 5(d), Fig. S6(e) in the ESM). As the crack extended into the MBNS/Ni_2Si assembly, it underwent a jagged deflection along the edge of the reinforcements, accompanied by bridging constraints (Figs. 5(e) and 5(f)). Notably, upon crack propagation into the GC/MBNS assembly, the crack was arrested after penetrating only the surface layer of GC (Fig. S6(f) in the ESM), demonstrating excellent crack energy dissipation. It was rare that such multiple-reinforced phases synergistically toughened the ceramic matrix from different dimensions (2D, 0D) and scales (nano, micron).

3.3 Electromagnetic wave absorption performance of DS@MBNS composites

Structured materials such as metamaterials and porous materials are favored by researchers in the electromagnetic wave absorption (EMA) area due to their multiple reflection pathways for

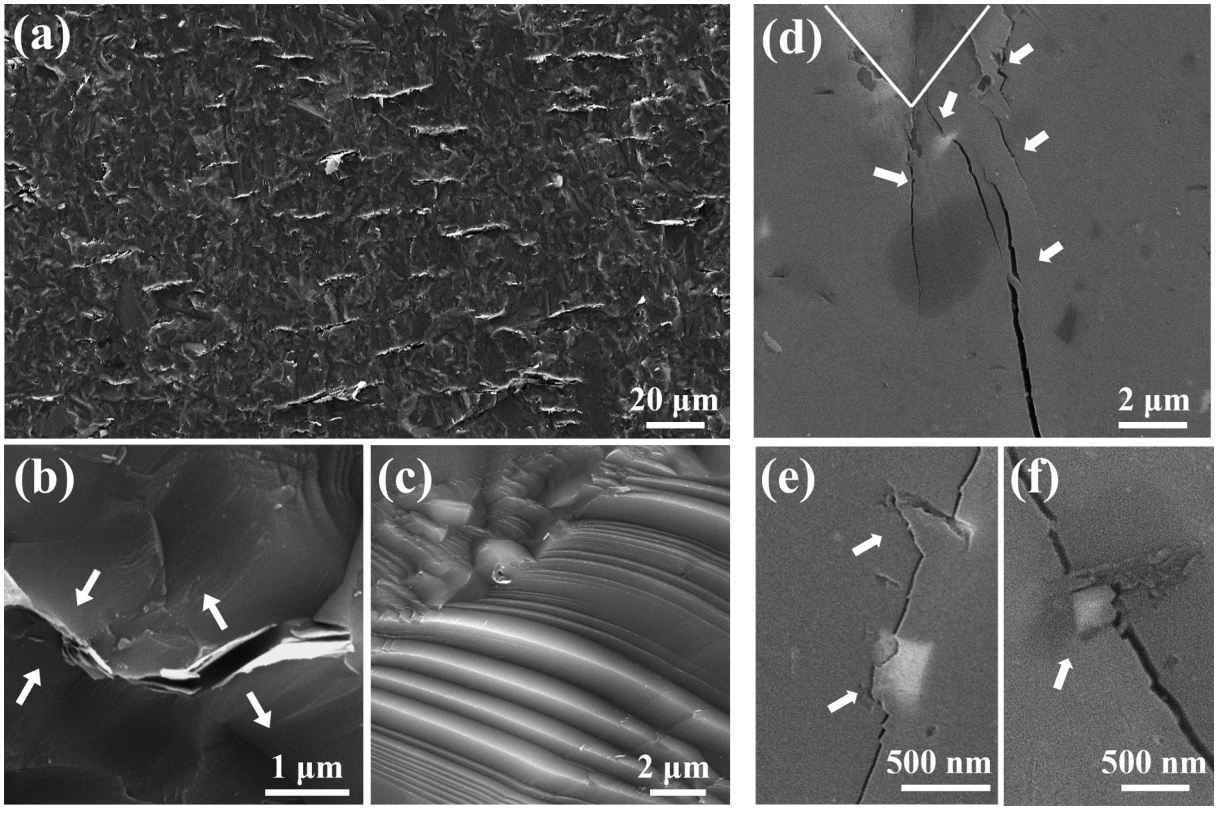

Fig. 5 Fracture morphologies and toughening mechanisms of DS@MBNS composites. (a) MBNS exhibiting a near-horizontal tearing morphology within the ceramic matrix. (b) Robust interfacial bonding between the MBNS and SiC matrix. (c) Evolution of stepped tear paths along fracture surfaces. (d) Crack bifurcation at indentation zones under tapered diamond loading. (e) Crack deflection induced by MBNS/Ni_2Si. (f) Reinforcement assembly bridging, effectively impeding crack propagation.

electromagnetic waves (EMW), lightweight nature, and high design flexibility. However, their intrinsic structural strength (strength, toughness, stiffness) is frequently compromised by purpose-driven structural design [37,38]. Consequently, under harsh service conditions, including high mechanical loads, extreme temperatures or pressures, and corrosive or radiative environments, their performance reliability becomes significantly degraded [39]. In this work, we explored a structurally robust EMA composite system by integrating exfoliated MBNSs within a dual-phase SiC matrix (DS). A waveguide-based, nondestructive testing method was employed to evaluate the EMA performance, ensuring high measurement fidelity. Reflection loss (RL), derived from transmission line and metal-backing theory, was used to quantify EMA performance. The effective absorption bandwidth (EAB), defined as the frequency range with RL ≤ −10 dB, indicates absorption of over 90% of the incident EMW.

Figure 6 presents the systematic evolution of the Ku-band (12.4–18.0 GHz) absorption performance for all specimens. A nonmonotonic trend was observed with increasing MBNS content: an initial decline in RL values followed by a substantial improvement (Figs. 6(a)–6(f)). The OS specimen, with a single-phase α-SiC matrix, achieved only weak absorption at 15.66 GHz with a high matching thickness of 4.56 mm, yielding an RL_{min} of −25.32 dB and an EAB of 1.57 GHz (Fig. 6(a)). Upon converting the OS matrix to DS, the control groups (DS, DS@2BN) without MBNSs displayed poor absorption (RL_{min} > −5 dB) (Figs. 6(b) and 6(c)). Although bulk h-BN addition slightly reduced the RL value of DS@2BN compared to DS, its large particle size resulted in a sparse matrix distribution, limiting performance enhancement. In contrast, exfoliated MBNSs introduced pronounced EMA improvements even at low concentrations. With only 1 wt% MBNS, the DS@1MBNS specimen achieved a substantial increase in an RL_{min} of −45.12 dB and an EAB of 1.77 GHz at a matching thickness similar to OS (Fig. 6(d)). Increasing the MBNS content to 2 wt%, the RL_{min} of the DS@2MBNS specimen decreased to −17.81 dB at a thickness of 1.00 mm, but its EAB increased to 2.22 GHz at 1.01 mm (Fig. 6(e)). Further increasing the MBNS content to 4 wt%, the DS@4MBNS specimen yielded a significant improvement of RL_{min} of −52.59 dB at 1.22 mm and an EAB_{max} of 5.6 GHz (covering the entire Ku-band) at 1.09 mm (Fig. 6(f), Fig. S7 in the ESM). Additionally, the RL absorption peaks were observed to shift toward lower frequencies with increasing absorber thickness, consistent with the quarter-wavelength matching theory (Fig. S7 in the ESM) [40]. Comparative plots of RL_{min} vs. EAB_{max} and absorber thickness for all specimens (Figs. 6(g) and 6(h)) demonstrated the continuous EMA improvement in EMA performance with structural and compositional optimization. Notably, the DS@4MBNS specimen exhibited the optimal overall performance. Finally, benchmarking against literature-reported Ku-band EMA materials revealed that our MBNS-reinforced SiC system not only surpassed many reported absorbers in terms of RL_{min} and EAB but also offered exceptional structural integrity, marking a significant advancement in high-performance, mechanically resilient EMA materials (Fig. 6(i), Table S7 in the ESM).

The relative complex permittivity ($\varepsilon_r = \varepsilon' - j\varepsilon''$) and complex permeability ($\mu_r = \mu' - j\mu''$) are fundamental parameters used to judge the dielectric and magnetic responses of composites under an electromagnetic field [41]. These parameters directly determine the EMW absorption characteristics of materials. where ε_r and μ_r are composed of real parts (ε' and μ') and imaginary parts (ε'' and μ''), which represent the storage and dissipation capacities for electric and magnetic energy, respectively. ε' and ε'' are represented by Eqs. (6) and (7) [42]:

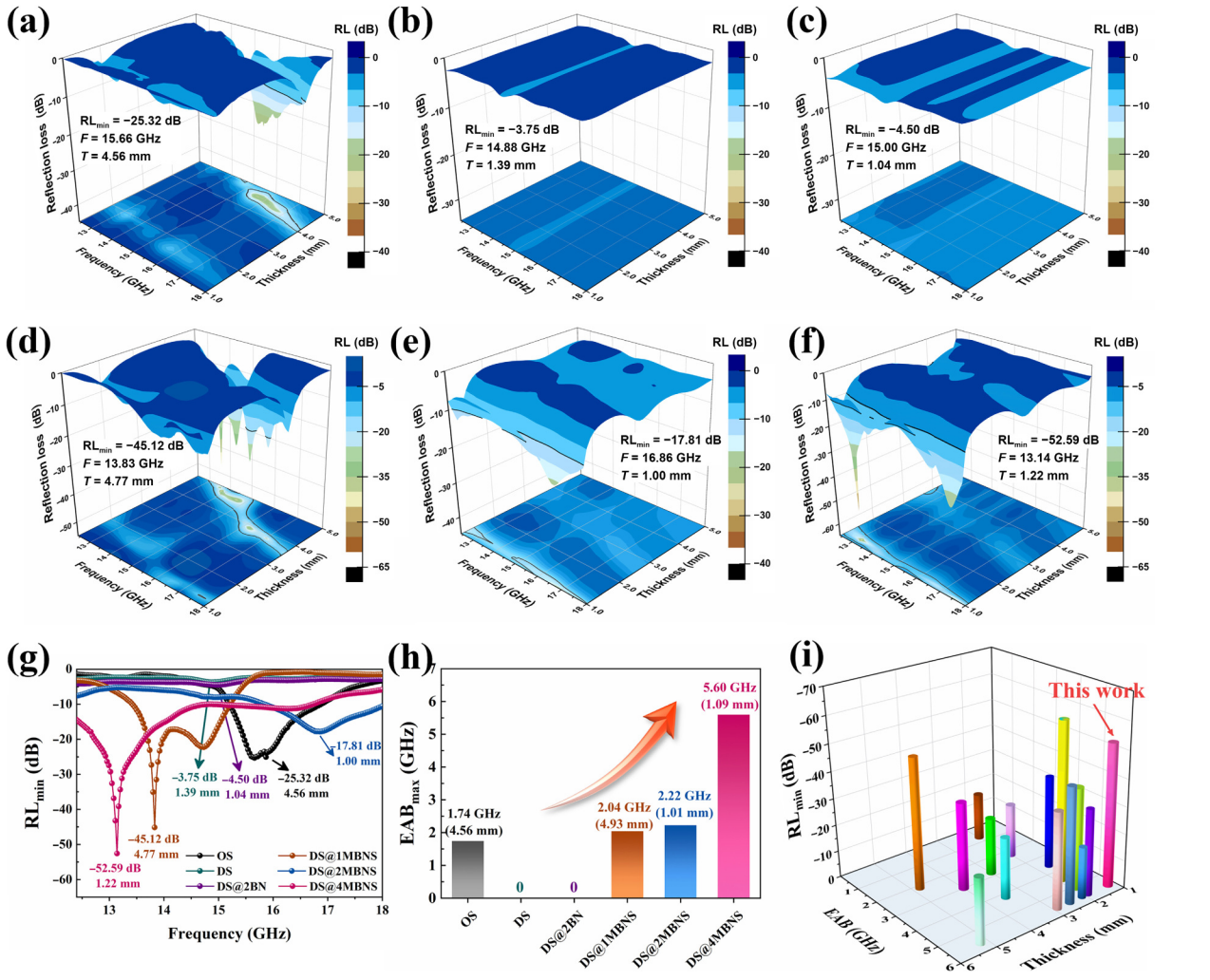

Fig. 6 Electromagnetic wave absorption performance of composite ceramics. 3D reflection loss (RL) mapping diagrams of (a) OS, (b) DS, (c) DS@2BN, (d) DS@1MBNS, (e) DS@2MBNS, and (f) DS@4MBNS. g Comparison of the minimum RL value (RL_{min}) curves for different specimens at the corresponding matched thickness. (h) Comparison of the maximum EAB range (EAB_{max}) for different specimens at the corresponding matched thickness. (i) Performance comparison of the optimum RL_{min}, EAB, and matching thickness of EMA absorbers in the Ku-band reported in the literature (Table S7 in the ESM). Note: *F* represents the frequency corresponding to the RL_{min}, and *T* represents the matching thickness of the specimen.

$$\varepsilon' = \varepsilon_\infty + \frac{\varepsilon_s - \varepsilon_\infty}{1 + (2\pi f)^2 \tau^2} \tag{6}$$

$$\varepsilon'' = \varepsilon_p'' + \varepsilon_c'' = \frac{2\pi f \tau (\varepsilon_s - \varepsilon_\infty)}{1 + (2\pi f)^2 \tau^2} + \frac{\sigma}{2\pi f \varepsilon_0} \tag{7}$$

where ε_∞, ε_s, τ, σ, ε_0, ε_c, and ε_p represent the high frequency limiting permittivity, static permittivity, polarization relaxation time, electrical conductivity, vacuum permittivity, conduction loss and polarization relaxation loss, respectively. As shown in Fig. 7(a), the initial OS specimen exhibited the lowest ε' values with nearly zero ε'', implying limited electric energy storage and negligible dielectric loss. This aligned with the typical behavior of nonpolymer-derived ceramics after high-temperature densification, where a reduction in intrinsic crystal defects, including grain boundaries, pores, and amorphous regions, during sintering leads to enhanced crystallinity. As a result, interfacial polarization and microwave scattering effects are suppressed, ultimately impairing the EMA performance [43,44].

In contrast, the DS matrix significantly improved ε' and ε'' values (particularly ε'') across the DS specimen group. Phase composition and microstructure analyses revealed that the DS matrix incorporated β-SiC stacking faults and twinning boundaries and abundant α/β-SiC grain interfaces (Figs. S7(a) and S7(c) in the ESM), contributing to enhanced polarization mechanisms. Additionally, Ni_2Si intermetallic and semigraphitic GC structures, located at grain boundaries and intragranular sites, respectively, formed a heterogeneous conductive network (Figs. 3(c) and 3(d), Figs. S4(b) and S4(e) in the ESM). These conductive and dielectric heterointerfaces collectively increased the dielectric constant and loss tangent ($\tan\delta(\varepsilon) = \varepsilon''/\varepsilon'$), enabling superior EMW dissipation relative to OS. It is well known that h-BN is recognized as an excellent wave-transparent material with low permittivity and loss, but thinner MBNS exhibit even lower dielectric losses due to reduced surface energy dissipation compared to bulk h-BN [45]. In DS@2BN, the limited and uneven dispersion of bulk h-BN weakens its contribution to the dielectric properties, yet a stronger frequency-dependent dispersion in ε' is observed compared to DS [46]. This led to abnormal $\tan\delta(\varepsilon)$ fluctuations in the high-frequency regions (Fig. S8(a) in the ESM). Obviously, MBNS incorporation into the DS matrix systematically reduced ε'' values to varying degrees, contributing to more tunable and balanced dielectric behavior (Fig. 7(a)).

Notably, all non-OS specimens exhibited multiple resonance peaks on their $\varepsilon'-\varepsilon''$ curves, which are attributed to

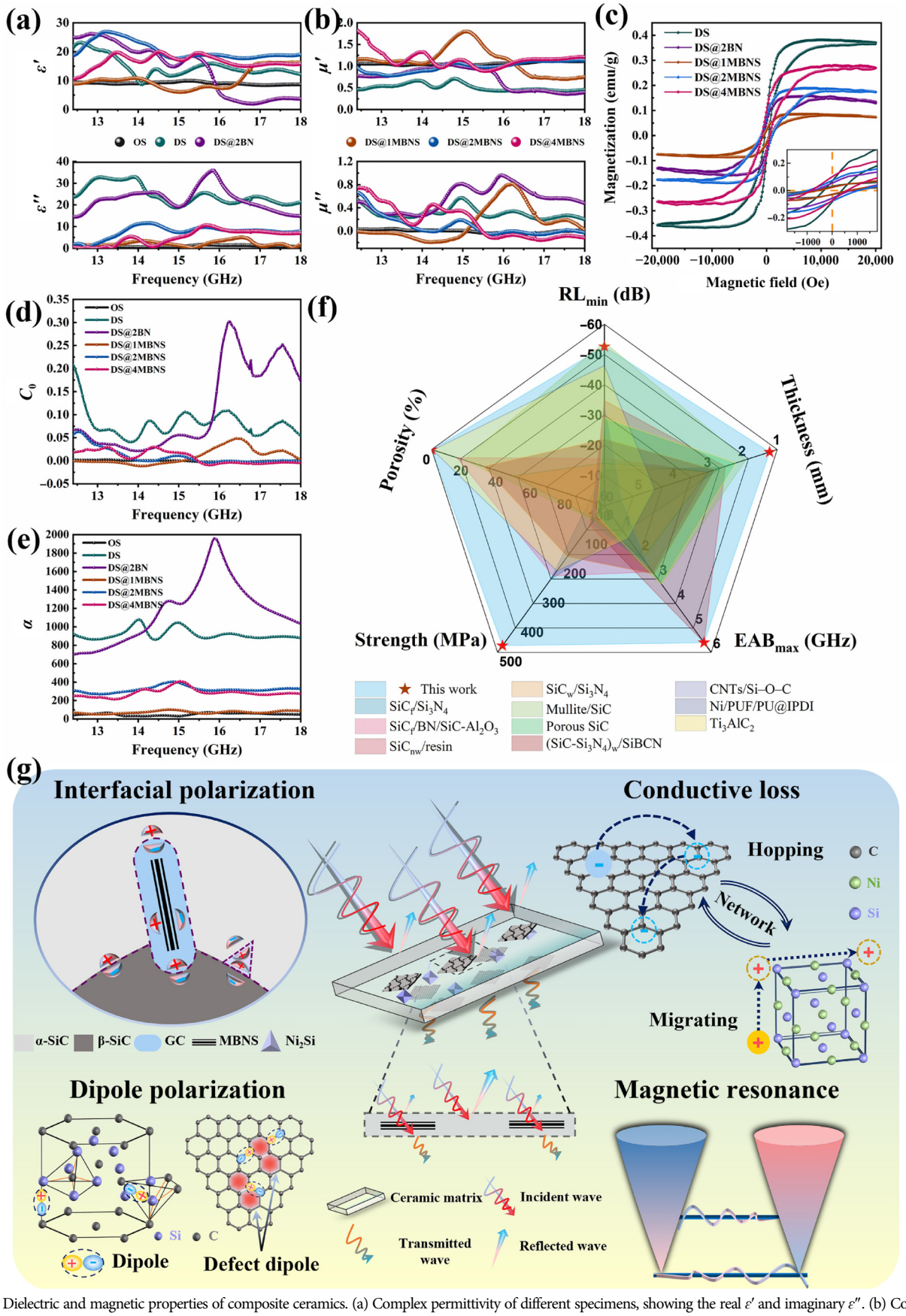

Fig. 7 Dielectric and magnetic properties of composite ceramics. (a) Complex permittivity of different specimens, showing the real ε' and imaginary ε''. (b) Complex permeability of different specimens, showing the real μ' and imaginary μ''. (c) Hysteresis loops of all specimens except OS, with insets displaying coercivity (H_c) magnitudes. (d) Eddy-current loss coefficients (C_o) as a function of frequency. (e) Attenuation constants (α) of the specimens. (f) Radar chart comparison of the reported structural-functionalized EMW absorbers in terms of mechanical strength, porosity, RL_{min}, EAB_{max}, and absorber thickness, listed in Table S8 in the ESM. (g) Schematic illustration of the EMW attenuation mechanism in DS@MBNS composites.

清華大学出版社 Tsinghua University Press | SciOpen

Maxwell–Wagner interfacial polarization and electromagnetic coupling under EM fields [47]. Specifically, in these multiphase systems (conductive Ni_2Si/GC and dielectric MBNS fillers/DS matrix), interfacial mismatch in conductivity, permeability, and permittivity led to localized charge accumulation. Under high-frequency excitation, rapid charge migration and relaxation at these interfaces generated distinct dielectric loss peaks. To further analyze the polarization relaxation behavior, Cole–Cole semicircle analysis based on Debye theory was conducted, where the ε'–ε'' relationship is expressed as Eq. (8) [48]:

$$\left(\varepsilon' - \frac{\varepsilon_s - \varepsilon_\infty}{2}\right)^2 + \left(\varepsilon''\right)^2 = \left(\frac{\varepsilon_s - \varepsilon_\infty}{2}\right)^2 \quad (8)$$

The Cole-Cole curves of all specimens exhibited multiple semicircular arcs (Fig. S9 in the ESM), where each arc corresponded to a distinct Debye relaxation process. This confirmed the coexistence of multiple polarization mechanisms, including defect-induced, dipolar, and interfacial polarization, which were responsible for the resonance peaks observed in the dielectric constant curves.

Given that the OS specimen was nonmagnetic, its real (μ') and imaginary (μ'') parts of complex permeability remained close to 1 and 0, respectively. In contrast, the other specimens displayed weak magnetic responses primarily due to the presence of Ni_2Si intermetallic compounds [24]. The μ' values decreased with increasing frequency, while the magnetic loss tangent ($\tan\delta(\mu) = \mu''/\mu'$) followed the μ'' trend (Fig. 7(b), Fig. S8(b) in the ESM). Similar multipeak resonance was also observed in the permeability curves. Notably, the DS@MBNS group exhibited higher average μ' but lower average μ'' values than the non-MBNS group. Furthermore, some DS@MBNS specimens showed slight negative μ'' values, implying minor magnetic energy radiation from the induced magnetic field, partially converted into electrical energy [49].

To further assess magnetic properties, room-temperature hysteresis loops were measured for all specimens except OS. The curves revealed that DS achieved the highest saturation magnetization (M_s) of 0.367 emu·g^{-1}, whereas introducing nonferromagnetic h-BN or MBNS reduced Ms collectively (Fig. 7(c)). However, in the DS@MBNS specimens, M_s increased with MBNS content, reaching 0.278 emu·g^{-1}. This enhancement was likely due to a more uniform Ni_2Si distribution in the matrix, which mitigated magnetic moment cancellation among adjacent particles, thereby enhancing the overall magnetization [50]. Moreover, the coercivity (H_c) of all specimens ranged from 300 to 1000 Oe, showing an inverse correlation with M_s (Fig. 7(c), inset). The relationship between initial permeability (μ_i) and M_s is described by Eq. (9) [51]:

$$\mu_i = \frac{M_s^2}{akH_cM_s + b\lambda\xi} \quad (9)$$

where the constants (a and b) are determined by the material's composition, while k represents a scaling factor. λ and ξ denote the magnetostriction coefficient and elastic strain parameter, respectively. The equations demonstrate that higher static M_s and lower H_c are conducive to enhancing permeability, thereby improving the material's dynamic magnetic loss in varying electromagnetic fields. Specifically, the DS@4MBNS specimen exhibited a favorable magnetic loss profile, with an average μ' of 1.15, an average $\mu'' > 0.15$, and a peak μ'' of 0.74. Magnetic losses in these composites primarily originate from hysteresis loss, eddy current loss, ferromagnetic resonance (natural and exchange), and domain wall resonance. Given the inherently weak magnetism of the material system, hysteresis loss is negligible, while domain wall motion and natural resonance effects typically manifest in low-frequency regimes (kHz–MHz and 2–10 GHz, respectively) [52]. Thus, eddy current loss and exchange resonance dominated the magnetic loss in this system. To distinguish between these mechanisms, the eddy current loss coefficient ($C_o = \mu''(\mu')^{-2}f^{-1} = 2\pi\mu_0 d^2\sigma$) was calculated and analyzed as a function of frequency (Fig. 7(d)). Herein, d and σ represents absorber thickness and electrical conductivity of the specimen, respectively. If C_o remains stable within a frequency range, eddy current loss prevails; otherwise, exchange resonance dominates.

For the DS specimen, pronounced C_o fluctuations across the Ku-band confirmed exchange resonance as the dominant loss mechanism. The DS@2BN and DS@1MBNS specimens with sparsely distributed BN sheets caused C_o fluctuations at high frequencies (15.5–18 GHz), while low-frequency regions (12.4–15.5 GHz) showed C_o stabilization, suggesting eddy current loss dominance below 15.5 GHz and exchange resonance above. As the MBNS content increased, the resonance peaks shifted toward lower frequencies in DS@2MBNS and DS@4MBNS, effectively reversing the dominant loss mechanism. These findings confirmed the role of Ni_2Si in imparting ferromagnetic properties for magnetic loss, while MBNS enabled tunable permeability and adaptive loss modulation.

Furthermore, the attenuation constant (α) and impedance matching (Z) are critical EMA performance metrics. α quantifies the material's EMW attenuation capacity, and $Z \approx 1$ ensures minimal EMW reflection at the surface. These parameters are expressed as Eqs. (10) and (11) [53,54]:

$$\alpha = \frac{\sqrt{2}\pi f}{c} \times \sqrt{(\mu''\varepsilon'' - \mu'\varepsilon') + \sqrt{(\mu''\varepsilon'' - \mu'\varepsilon')^2 + (\mu''\varepsilon'' + \mu''\varepsilon')^2}} \quad (10)$$

$$z = \left|\frac{Z_{in}}{Z_0}\right| = \sqrt{\left|\frac{\mu_r}{\varepsilon_r}\right|} \tanh\left(j\frac{2\pi f d}{c}\sqrt{\mu_r\varepsilon_r}\right) \quad (11)$$

where Z_{in}, Z_0, d, and c represent the absorber's input impedance, free-space impedance, absorber thickness, and speed of light in vacuum, respectively. As shown in Fig. 7(e), the attenuation constants (α) of all specimens were significantly enhanced after OS matrix modification. However, despite their elevated α values, the DS and DS@2BN specimens suffered from severe impedance mismatch, which resulted in substantial reflection of incident EM waves and, consequently, poor absorption performance (Figs. 6(b) and 6(c), Fig. S8(c) in the ESM). In contrast, the DS@MBNS series not only achieved higher α values but also optimized impedance matching, thereby delivering exceptional EMA performance (Figs. 6(g) and 6(h)).

To comprehensively illustrate the EMW attenuation mechanism of DS@MBNS composites, a schematic model is presented in Fig. 7(g). Importantly, the EMA tests were conducted under nondestructive conditions, ensuring that the specimen integrity and MBNS distribution were identical to those in the mechanical property test. The performance enhancement was attributed to the synergistic coupling of mechanical robustness and electromagnetic functionality. This was achieved by modifying the intrinsically nonmagnetic and weakly dielectric OS matrix and introducing a multiple-reinforcement phase, which simultaneously enhanced structural stability and introduced critical electromagnetic properties. MBNS, a more efficient wave-transparent filler compared to conventional h-BN, enabled

efficient EMW transmission under high-frequency fields. Unlike traditional EMW attenuation materials that typically require high porosity in the matrix, DS@MBNS composites possessed high density and a lack of internal voids (Fig. 4(d), Table S6 in the ESM), thereby hindering multiple scattering of EMW within the ceramic matrix. In this case, MBNS not only optimized impedance matching to facilitate EMW penetration but also integrated various loss mechanisms to attenuate and absorb EMW [55]. This partially compensated for the deficiency of EMW dissipation pathways in highly dense ceramics. The dominant attenuation mechanisms involved dielectric loss (primarily polarization and conductive loss) and were supplemented by magnetic loss (eddy current loss, resonance modes) [56]. Polarization loss, dominated by interfacial and dipole polarization, originated from abundant interfaces, microstructural defects, and intrinsic dipoles in DS@MBNS, which acted as polarization sites to dissipate energy via cyclic polarization/depolarization under alternating electric fields [57,58]. Conductive loss arose from electron hopping and migration through the Ni_2Si/GC-dominated conductive network. Additionally, Ni_2Si contributed to ferromagnetic behavior, inducing magnetic loss via eddy currents and exchange resonance. The synergy of these mechanisms achieved the low RL_{min} and broad EAB observed in DS@MBNS composites.

To highlight the dual advantages of structural integrity and electromagnetic functionality, we benchmarked the DS@MBNS composite against previously reported systems, comparing metrics such as flexural strength, porosity, RL_{min}, EAB, and absorber thickness (Fig. 7(f), Table S8 in the ESM). These properties are of critical importance for emerging applications in lightweight aerospace components, precision-packaged electronics, and structural-functional armor requiring balanced strength and wave absorption [43,59]. The radar chart comparison revealed that many prior material systems suffered from performance extremization, failing to simultaneously achieve high strength and EMA efficacy. Remarkably, the DS@MBNS composite developed in this work demonstrated both outstanding structural strength and excellent EMA performance.

4 Conclusions

In summary, we developed a scalable, cost-efficient strategy to fabricate structurally robust modified boron nitride nanosheets (MBNSs) via a protective exfoliation approach and demonstrated their dual role in reinforcing SiC ceramics and enhancing electromagnetic wave absorption (EMA) performance. An effective modification strategy for the MBNS-dominated composite reinforcement phase and DS matrix was innovatively designed. By introducing a tailored precursor transformation during sintering, a hierarchical composite architecture was formed, comprising a self-associated dual-phase α/β-SiC (DS) ceramic matrix, horizontally aligned 2D-MBNS, and diffusely distributed 0D-Ni_2Si/GC phases. This architecture significantly improved the ceramic matrix's load-bearing and stress-transfer capacity through multiple toughening mechanisms, including crack bifurcation, deflection, and bridging. The optimized DS@4MBNS composite achieved ~95% improvement in flexural strength and ~50% enhancement in fracture toughness. Simultaneously, this optimized composite showed exceptional EMA performance with an RL_{min} of –52.59 dB at 1.22 mm and an EAB_{max} of 5.6 GHz covering the entire Ku-band at 1.09 mm, attributed to the synergistic effects of dielectric and magnetic loss. Our results demonstrate the effective integration of mechanical strength and EMA functionality, offering a promising pathway for advanced structural–electromagnetic materials.

Acknowledgements

This work was financially supported by the National Natural Science Foundation of China (Grant No. 52272063), Aeronautical Science Foundation of China (Grant No. 2024Z055056001), and Key Research and Development Program of Jiangxi Province (Grant No. 20243BBI91006).

Availability of data and materials

The data that support the findings of this study are available from the corresponding author upon reasonable request.

Competing interests

The authors have no competing interests to declare that are relevant to the content of this article.

Electronic Supplementary Material

Supplementary material is available in the online version of this article at https://doi.org/10.26599/JAC.2025.9221234.

References

[1] Amontree J, Yan XZ, DiMarco CS, *et al.* Reproducible graphene synthesis by oxygen-free chemical vapour deposition. *Nature* 2024, **630**: 636–642.
[2] Park JM, Cao Y, Xia LQ, *et al.* Robust superconductivity in magic-angle multilayer graphene family. *Nat Mater* 2022, **21**: 877–883.
[3] Brunet Cabré M, Spurling D, Martinuz P, *et al.* Isolation of pseudocapacitive surface processes at monolayer MXene flakes reveals delocalized charging mechanism. *Nat Commun* 2023, **14**: 374.
[4] Liu L, Ying GB, Jiang QG, *et al.* Ultra-high-temperature application of MXene: Stabilization of 2D $Ti_3C_2T_x$ for cross-scale strengthening and toughening of 3D TiC. *J Adv Ceram* 2024, **13**: 1–10.
[5] Conti S, Calabrese G, Parvez K, *et al.* Printed transistors made of 2D material-based inks. *Nat Rev Mater* 2023, **8**: 651–667.
[6] Yang YC, Song ZG, Lu GY, *et al.* Intrinsic toughening and stable crack propagation in hexagonal boron nitride. *Nature* 2021, **594**: 57–61.
[7] Cheng YM, Han YX, Zhang W, *et al.* Gram-scale synthesis of boron nitride nanosheets by salt-template method for anticancer drug delivery. *Chem Eng J* 2022, **437**: 135304.
[8] Wang ZY, Yan X, Hou QF, *et al.* Scalable high yield exfoliation for monolayer nanosheets. *Nat Commun* 2023, **14**: 236.
[9] Zhou YC, Xu LS, Liu MS, *et al.* Viscous solvent-assisted planetary ball milling for the scalable production of large ultrathin two-dimensional materials. *ACS Nano* 2022, **16**: 10179–10187.
[10] Han YX, Ruan KP, Gu JW. Multifunctional thermally conductive composite films based on fungal tree-like heterostructured silver nanowires@boron nitride nanosheets and aramid nanofibers. *Angew Chem Int* 2023, **62**: 202216093.
[11] Ma LS, Zhang X, Pu BW, *et al.* Achieving the strength–ductility balance of boron nitride nanosheets/Al composite by designing the synergistic transition interface and intragranular reinforcement distribution. *Compos Part B Eng* 2022, **246**: 110243.
[12] Li ZH, Liu L, You X, *et al.* Cooperative enhancement of mechanical and tribological properties through tailoring TiN transition interface in boron nitride nanosheets reinforced copper composites. *Rare Metals* 2024, **43**: 5202–5215.
[13] Duan XM, Yang ZH, Chen L, *et al.* Review on the properties of hexagonal boron nitride matrix composite ceramics. *J Eur Ceram Soc* 2016, **36**: 3725–3737.
[14] Li T, Gu SY, Xu ZK, *et al.* Effect of hexagonal boron nitride content on the anisotropy of hot-press-sintered AlN/BN composite ceramics. *Ceram Int* 2024, **50**: 29486–29493.
[15] Xia Y, Su Y, Huang JT, *et al.* Design and preparation of multiple, multidimensional and multiscale Ni/GC/CNTs/MLGs toughened phases. *Ceram Int* 2024, **50**: 36320–36329.
[16] Wang X, Xia Y, Huang JT, *et al.* A facile strategy for large-scale

production of 2D nanosheets exfoliated by three-roll milling. *J Adv Ceram* 2024, **13**: 11–18.
[17] Zeng QH, Chen XW. Combustor technology of high temperature rise for aero engine. *Prog Aerosp Sci* 2023, **140**: 100927.
[18] Song CK, Ye F, Cheng LF, *et al.* Long-term ceramic matrix composite for aeroengine. *J Adv Ceram* 2022, **11**: 1343–1374.
[19] Sun C, Huang YJ, Shen Q, *et al.* Embedding two-dimensional graphene array in ceramic matrix. *Sci Adv* 2020, **6**: eabb1338.
[20] Ma J, Zhang H, Yang B, *et al.* Ultrathin graphite-encapsulated Y2Co17 nanostructures with good structural stability and switchable microwave absorption. *Rare Metals* 2025, **44**: 8863–8883.
[21] Liu MQ, Huang JT, Meng HT, *et al.* A novel approach to prepare graphite nanoplatelets exfoliated by three-roll milling in phenolic resin for low-carbon MgO–C refractories. *J Eur Ceram Soc* 2023, **43**: 4198–4208.
[22] Zhang TY, Li Y, Li LH, *et al.* Symmetry-breaking triggered by atomic tungsten for largely enhanced piezoelectric response in hexagonal boron nitride. *Nano Energy* 2022, **99**: 107375.
[23] Xia Y, Liu LY, Huang JT, *et al.* A new strategy to prepare MLG-SiC_w/SiC_p composites via three-roll milling exfoliation and catalytical-conversion for advanced refractories. *Ceram Int* 2024, **50**: 49853–49861.
[24] Gogebakan M, Kursun C, Gunduz KO, *et al.* Microstructural and mechanical properties of binary Ni–Si eutectic alloys. *J Alloys Compd* 2015, **643**: S219–S225.
[25] Sun J, Zhang JD, Zhang X, *et al.* High strength mullite-bond SiC porous ceramics fabricated by digital light processing. *J Adv Ceram* 2024, **13**: 53–62.
[26] Li WX, Pang HJ, Zhang ZX, *et al.* Core–shell SiC_w@TiC composite whisker-reinforced Al_2O_3 ceramics: Preparation, properties, and toughening mechanisms. *J Adv Ceram* 2025, **14**: 9221093.
[27] Cheng Z, Liang JB, Kawamura K, *et al.* High thermal conductivity in wafer-scale cubic silicon carbide crystals. *Nat Commun* 2022, **13**: 7201.
[28] Ren B, Deng YM, Jia YJ, *et al.* Achieving broadband electromagnetic absorption at a wide temperature range up to 1273 K by metamaterial design on polymer-derived SiC-BN@CNT ceramic composites. *Chem Eng J* 2023, **478**: 147251.
[29] Zhou J, Zhang YH, Mao QZ, *et al.* Optimizing electrochemical performances of ultra-high nickel layered cathodes through gradient doping and solid electrolyte coating. *Tungsten* 2025, https://doi.org/10.1007/s42864-025-00346-9.
[30] Cao Y, Nyborg L, Jelvestam U. XPS calibration study of thin-film nickel silicides. *Surf Interface Anal* 2009, **41**: 471–483.
[31] Mondal I, Hausmann JN, Vijaykumar G, *et al.* Nanostructured intermetallic nickel silicide (pre)catalyst for anodic oxygen evolution reaction and selective dehydrogenation of primary amines. *Adv Energy Mater* 2022, **12**: 2200269.
[32] Li F, Feng YX, Li ZW, *et al.* Rational kinetics control toward universal growth of 2D vertically stacked heterostructures. *Adv Mater* 2019, **31**: 1901351.
[33] Tang H, Cheng Y, Yuan XH, *et al.* Toughening oxide glasses through paracrystallization. *Nat Mater* 2023, **22**: 1189–1195.
[34] Chen JJ, Sun QC, Chen J, *et al.* Mechanical and tribological properties of *h*-BN/ZrO_2/SiC solid-lubricating ceramic composites. *Tribol Int* 2021, **160**: 107061.
[35] Qian WF, Ning BK, Wang S, *et al.* Hierarchically structured ceramic coatings based on zirconia and magnesium oxide with high toughness. *Adv Funct Mater* 2025, **35**: 2418312.
[36] Texier D, Stinville JC, Echlin MP, *et al.* Short crack propagation from cracked non-metallic inclusions in a Ni-based polycrystalline superalloy. *Acta Mater* 2019, **165**: 241–258.
[37] Ning Y, Zeng XJ, Huang J, *et al.* Multifunctional electromagnetic responsive porous materials synthesized by freeze casting: Principles, progress, and prospects. *Adv Funct Mater* 2025, **35**: 2414838.
[38] Liu SK, Zhou YM, Zhang FX, *et al.* A novel full-band microwave absorber based on scattering enhanced prism-honeycomb nested structure. *Adv Funct Mater* 2025, **35**: 2422666.
[39] Hao B, Zhang Y, Si HX, *et al.* Multiscale design of dielectric composites for enhanced microwave absorption performance at elevated temperatures. *Adv Funct Mater* 2025, **35**: 2423897.
[40] Song LM, Wang LN, Chen YQ, *et al.* Engineered core–shell SiC@SiO_2 nanofibers for enhanced electromagnetic wave absorption performance. *Small* 2024, **20**: 2407563.
[41] Wu CW, Zhang F, Zhi Q, *et al.* From binary to ternary and back to binary: Transition of electromagnetic wave shielding to absorption among MAB phase Ni_3ZnB_2 and corresponding binary borides $Ni_{n+1}B_n$ (n = 1, 3). *J Adv Ceram* 2023, **12**: 2101–2111.
[42] Li LY, Zhang M, Jiang M, *et al.* High entropy ceramics for electromagnetic functional materials. *Adv Funct Mater* 2025, **35**: 2416673.
[43] Li DX, Jia DC, Yang ZH, *et al.* Principles, design, structure and properties of ceramics for microwave absorption or transmission at high-temperatures. *Int Mater Rev* 2022, **67**: 266–297.
[44] Yu GY, Shao GF, Xu RP, *et al.* Metal–organic framework-manipulated dielectric genes inside silicon carbonitride toward tunable electromagnetic wave absorption. *Small* 2023, **19**: 2304694.
[45] Laturia A, van de PML, Vandenberghe WG. Dielectric properties of hexagonal boron nitride and transition metal dichalcogenides: From monolayer to bulk. *npj 2D Mater Appl* 2018, **2**: 6.
[46] Hou YZ, Yang W, Zhong C, *et al.* Thermostable SiCO@BN sheets with enhanced electromagnetic wave absorption. *Chem Eng J* 2019, **378**: 122239.
[47] Pan F, Cai L, Shi YY, *et al.* Heterointerface engineering of β-chitin/carbon nano-onions/Ni–P composites with boosted Maxwell–Wagner–Sillars effect for highly efficient electromagnetic wave response and thermal management. *Nano-Micro Lett* 2022, **14**: 85.
[48] Tao JQ, Yan Y, Zhou JT, *et al.* Anionic high-entropy doping engineering for electromagnetic wave absorption. *Nat Commun* 2025, **16**: 3163.
[49] Xiang ZN, Xu BK, He QC, *et al.* Synergistic magnetic/dielectric loss of Fe_3Si/SiC composites for efficient electromagnetic wave absorption. *Chem Eng J* 2023, **457**: 141198.
[50] Bai GH, Liu JH, Bandaru S, *et al.* Interfacial reaction enhanced liquid-phase sintering of metal/oxide soft magnetic composite. *Adv Funct Mater* 2023, **33**: 2303951.
[51] Yang BT, Fang JF, Xu CY, *et al.* One-dimensional magnetic FeCoNi alloy toward low-frequency electromagnetic wave absorption. *Nano Micro Lett* 2022, **14**: 170.
[52] Shu JC, Cao WQ, Cao MS. Diverse metal–organic framework architectures for electromagnetic absorbers and shielding. *Adv Funct Mater* 2021, **31**: 2100470.
[53] Li MR, Li W, Wang YX, *et al.* Entropy-driven microwave absorption enhancement in hexagonal $(Ba_{1/3}Sr_{1/3}Ca_{1/3})FeO_3$ perovskite. *J Adv Ceram* 2025, **14**: 9221059.
[54] Hou YL, Sheng ZZ, Fu C, *et al.* Hygroscopic holey graphene aerogel fibers enable highly efficient moisture capture, heat allocation and microwave absorption. *Nat Commun* 2022, **13**: 1227.
[55] Geng TB, Yu GY, Shao GF, *et al.* Enhanced electromagnetic wave absorption properties of ZIF-67 modified polymer-derived SiCN ceramics by *in situ* construction of multiple heterointerfaces. *Rare Metals* 2023, **42**: 1635–1644.
[56] Yu GY, Shao GF, Xu ZL, *et al.* Hierarchical interface-engineered magnetic graphene-sicn aerogels via stepwise confinement strategy for low-frequency and broadband microwave absorption. *J Adv Ceram* 2025: 9221187.
[57] Gai LX, Wang YH, Wan P, *et al.* Compositional and hollow engineering of silicon carbide/carbon microspheres as high-performance microwave absorbing materials with good environmental tolerance. *Nano-Micro Lett* 2024, **16**: 167.
[58] Huang XG, Guan JP, Feng YJ, *et al.* Mn and O defect modulation in birnessite creates multiplicate polyhedra to improve dielectric and magnetic losses. *Cell Rep Phys Sci* 2025, **6**: 102350.
[59] Wang WC, Wang LY, Huang J, *et al.* Multi-heterointerface lightweight ceramics achieving temperature-insensitive dielectric properties for high-temperature electromagnetic wave effective absorption. *J Adv Ceram* 2025, **14**: 9221135.